npj | climate and atmospheric science

Article

Published in partnership with CECCR at King Abdulaziz University

https://doi.org/10.1038/s41612-024-00656-8

Anomalously weak intensity of tropical cyclones striking eastern China over the past two millennia

Yang Yang[1,2], Vittorio Maselli[3], Liang Zhou[4] ✉, Jianhua Gao[5], Ya Gao[6], Ya Ping Wang[5,7], Jianjun Jia[7] & Shu Gao[5] ✉

Anthropogenic climate warming is predicted to increase the intensity of global tropical cyclones (TCs) on decadal timescales, known as the 'temperature-TC intensity' paradigm. However, no proxy is currently available to directly quantify TC intensity in the northwestern Pacific region over centennial to millennial timescales. Here, we reconstruct the intensity of past TCs inferred from event-beds detected in two sedimentary systems in eastern China spanning approximately 1910 to 645 yr BP using an instrumental-calibrated technique, thereby encompassing a sufficiently wide range of temperatures to test the paradigm in the time domain. Intriguingly, our two intensity indices, based on flooding depth and wind speed, provide the initial quantitative evidence that TC intensity in eastern China has been anomalously weak since around 1485 ± 45 yr BP, with a reduction of approximately 30 ± 8% in intensity, despite no concurrent temperature shift. This reduction appears to have been pre-conditioned by a combined influence of a weaker El Niño-Southern Oscillation, a stronger Atlantic Meridional Overturning Circulation, and an increased level of Saharan dust. We suggest that the magnitudes of these factors may have crossed a tipping point and have not reverted to their pre-shift levels since that time, resulting in their impact on TC intensity exceeding that of temperature by triggering changes in the oceanic and atmospheric state within the tropical Pacific region where TCs originate.

Tropical cyclones (TCs) are one of the most catastrophic atmospheric events, characterized by strong winds, heavy rainfall and storm surges. Intense TCs cause devastating losses to human life and property, particularly in the coastal regions of the most active TC basins, such as the northwestern Pacific and North Atlantic[1–3]. The question of how TC activity will respond to future climate warming is increasingly drawing the attention of science community, although significant uncertainty still remains (e.g., refs. 4–7). Observational records (e.g., refs. 8–10) and model simulations (e.g.[6,11,12]) indicate that climate warming will increase the intensity of global TCs, potentially suggesting a 'temperature-TC intensity' paradigm of anthropogenic climate change. Balanced against this, an alternative view proposes that the increased cyclone intensity is related to natural oscillations in the atmospheric-oceanic system[13–15]. Nevertheless, the limited length of observation records and the relatively low level of confidence in future frequency projections[16–18] pose significant challenges to testing these hypotheses.

Coastal sedimentary archives offer a means to quantify historical fluctuations in TC activity and to uncover the main climate drivers, thus providing an alternative way to test these hypotheses. In the past few decades, various records of Holocene TC activity from the Atlantic, Pacific, and Indian oceans have been reported (e.g., refs. 19–25). These studies have primarily focused on detecting long-term frequency patterns of TC activity and associated climate forcings[26–30]. However, few pre-modern reconstructions have been used to understand the magnitude of past variations in

[1]School of Marine Science and Engineering, Nanjing Normal University, Nanjing, China. [2]Key Laboratory of Coastal Salt Marsh Ecosystems and Resources, Ministry of Natural Resources, Nanjing, China. [3]Department of Chemical and Geological Sciences, University of Modena and Reggio Emilia, Modena, Italy. [4]School of Geography, Geomatics and Planning, Jiangsu Normal University, Xuzhou, China. [5]School of Geography and Ocean Science, Ministry of Education Key Laboratory for Coast and Island Development, Nanjing University, Nanjing, China. [6]School of Marine Sciences, Sun Yat-sen University, Zhuhai, China. [7]State Key Laboratory of Estuarine and Coastal Research, School of Marine Sciences, East China Normal University, Shanghai, China. ✉e-mail: geolzhou@jsnu.edu.cn; shugao@nju.edu.cn

TC intensity (e.g., refs. 31–34), resulting in an incomplete picture of the long-term behavior of TC activity.

In coastal and marine settings, TCs are able to deposit coarse-grained sediments in areas typically experiencing finer sediment deposition as a result of storm surge. These TC-related sediment layers, referred to as TC-event-beds, can be used to infer the energy of historical TC events considering specific assumptions on past sea levels, sediment availability, and local geomorphology[35–37]. To enhance the precision of TC intensity reconstructions for specific areas, it is important to quantify the sedimentological characteristics of modern TC-event-beds for which the atmospheric and marine conditions (e.g., storm surge height and wind speed, etc.) are known. Quantification of TC-event-bed intensity begins with a comparison of modern TC intensity with the thickness, distribution, and grain size of the event beds[19,37,38]. Numerical models have also been developed to help constrain the intensity of TC-event-beds[31,33,39]. For example, an inverse modeling approach (i.e., a simple advection-settling model) tested only by a limited number of modern TC-induced overwash layers has been proposed to quantify the magnitude of past TC-event-beds based on the height of storm surge[31], and has been successfully applied at several landfall locations containing TC deposits (e.g.[32,40–42]). However, many of these conventional intensity reconstructions lack precise calibration against high-resolution instrumental records, as they do not span the entire period of the event bed records. This makes it challenging to make a direct quantitative comparison between the modern instrumental record and the long-term TC record. So far, the variability and driving mechanisms of past TC intensity remain highly uncertain, creating an urgent need for reliable proxy reconstructions of TC intensity on centennial to millennial scales. In contrast to the North Atlantic[31,33] and Australia[20,39], no-millennial-scale record is currently available to directly quantify TC intensity in the northwestern Pacific region.

In this study, we introduce a 2000-year-long record of TC intensity from two sites in eastern China, namely, the Jiangsu tidal flats and the Zhejiang-Fujian mud belt (Fig. 1). The deposition of muddy sediments at these sites has been both rapid and continuous over the past millennia[43], enabling the reconstruction of historical TC intensity using an instrumental-calibrated technique. Specifically, we used TC intensity indices based on flow depth and wind speed (TCI_*fd* and TCI_*ws*) to quantify TC intensity at the Jiangsu tidal flats and the Zhejiang-Fujian mud belt, respectively. By integrating instrumental records and existing paleoclimate records, we evaluate the magnitude of past variations in TC intensities and associated climate forcings over the last 2000 years.

Results

TC intensity indices

Cores SA and YC01 were retrieved from the Jiangsu tidal flats, while core ZM01 was obtained from the Zhejiang-Fujian mud belt. As reported by Yang et al.[30] core SA recorded 11 event beds spanning from 1941 to 2014 CE, corresponding to the 11 recent TCs that have impacted the Jiangsu coast (Supplementary Fig. 1 and Supplementary Table. 1). While not all of these 11 TCs directly hit the Jiangsu coast, they all caused storm surges along the coast due to their large maximum wind radius. These storm surges were recorded by a tide gauge station (Supplementary Table. 1) and ultimately contributed to the formation of the TC event layer on the tidal flats. The significant agreement between the event beds in core SA and recent TCs (Supplementary Fig. 1) strengthens our confidence in interpreting the event beds as the deposits left by TCs. TC-event-beds in core SA demonstrate a gradual-coarsening succession of sediment grain size from the upper part to the lower part of the tidal flats (Supplementary Table. 1). This suggests that the difference in grain size of TC-event-beds in different parts of the tidal flats could potentially be attributed to the influence of water depth on the transport distance. To verify this inference, we investigated the variation of grain size with seaward distance using high-accuracy positional data from two sections of the Jiangsu modern tidal flats (Fig. 1b) and the corresponding sediment grain size of surficial sediments. The results show that the mean grain size (Mz) and D90 of the P1 and P2 sections also exhibit a trend of coarsening toward the sea (Fig. 2c). Moreover, a strong logarithmic relationship was observed between D90 and relative distance (starting from the 2008 seawall). This finding, depicted in Fig. 2c, sheds light on how D90 and transport distance are connected for the TC-event-beds in different parts of the modern tidal flats.

To enhance the advection-settling model (A-S model), we initially calculated the settling velocities and depth-averaged flow velocities for the grain sizes characterizing the 11 TC-event-beds in core SA. Using Eq. 2 (see Methods), we then integrated the instrumental TCI_*fd* to compute the transport distances of these 11 TC-event-beds. As these event beds correspond to sediment on different parts of the tidal flats (Supplementary Table. 1), we were able to determine the transport distances of the TC-event-beds in each area. The transport distances for the upper, middle, and lower parts of the tidal flats were approximately 5715 ± 428 m, 3250 ± 461 m, and 2663 ± 272 m (Supplementary Fig. 2), respectively, which exhibited an expected logarithmic relationship with the corresponding D90 values (Fig. 2d). For core YC01 in the Jiangsu coast, we selected appropriate transport distances to reconstruct TCI_*fd* for the 36 TC-event-beds from different parts of the tidal flats[30]. We also adjusted the reconstructed TCI_*fd* for the

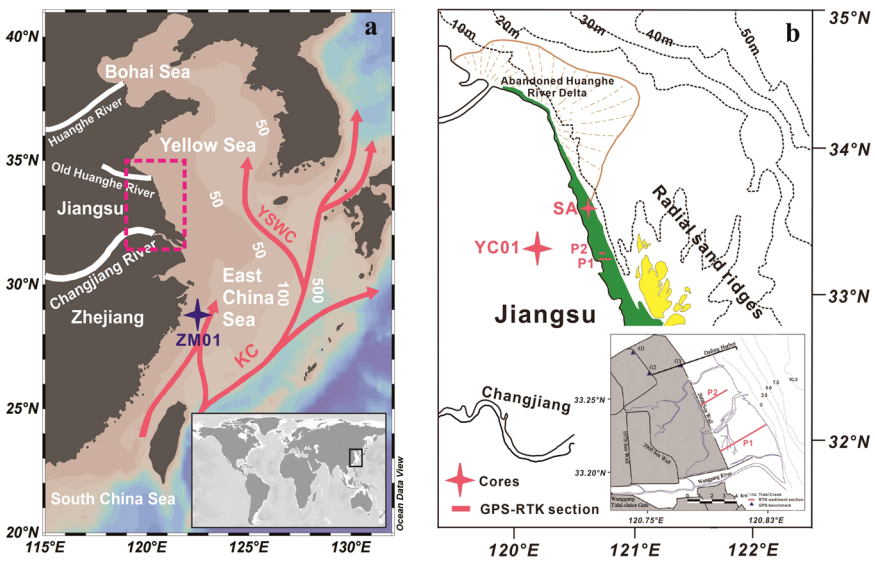

Fig. 1 | Site location. Maps showing (**a**) the study area and core ZM01, and (**b**) the locations of cores YC01 and SA, and the GPS–RTK sections (P1 and P2). KC: Kuroshio Current; YSWC: Yellow Sea Warm Current. The white lines (**a**), and green and yellow areas (**b**) represent the major rivers discharging into the sea, modern tidal flats and exposed sand ridges, respectively.

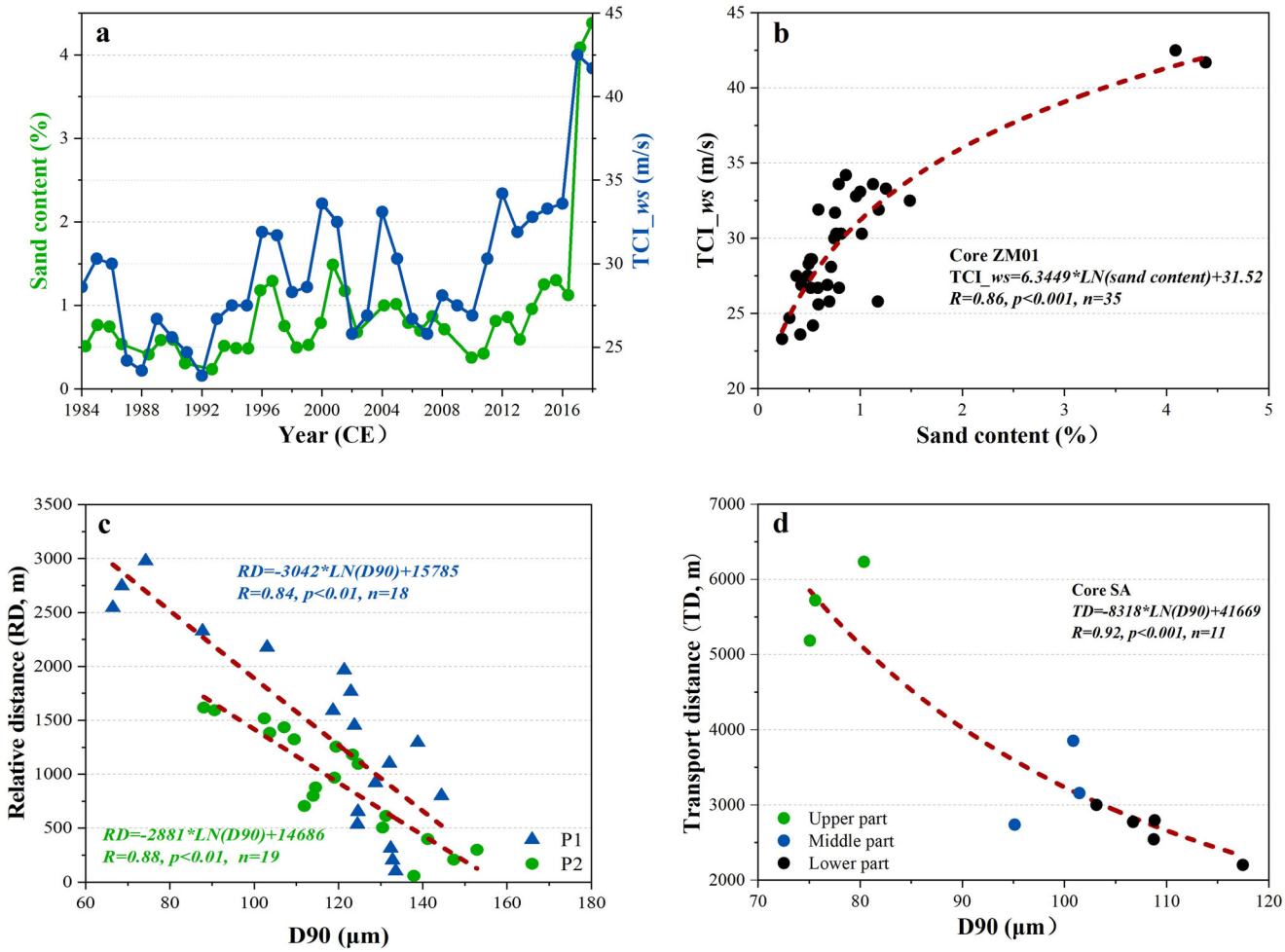

Fig. 2 | Establishment of TC intensity indices. Comparison (**a**) and correlation (**b**) of the sand content of core ZM01 with the instrumental TC wind speed (TCI_*ws*) affecting the Zhejiang coast (1984–2018 CE). The empirical relationships (**c**) between D90 and relative distance for P1 and P2 sections, and (**d**) between D90 and transport distance for TC-event-beds in core SA, both on the Jiangsu tidal flats.

sea level change off the Jiangsu coast[44]. Furthermore, we utilized the developed wind speed-based TC intensity index (TCI_*ws*; Fig. 2a, b) to reconstruct TC intensity for core ZM01 located at the Zhejiang-Fujian mud belt (see Eq. 3 in "Methods" section).

To assess the accuracy of the two intensity indices, we directly compared the instrumental TC intensity with these two indices (Supplementary Fig. 3). We first reconstructed the TCI_*fd* of 11 TC-event-beds in core SA and compared them with corresponding instrumental TC flow depths affecting the Jiangsu coast. We, therefore, reconstructed the TCI_ws of core ZM01 for the period of 1984 to 2018 CE and compared them with the instrumental annual maximum TC wind speed affecting the Zhejiang coast. The results indicated a small relative error, on average of 6.1% and 6.2% for the two indexes, respectively, demonstrating that they have significant potential to quantify TC intensity for the Jiangsu tidal flats and Zhejiang-Fujian mud belt, respectively.

Study period and TC intensity

The top 1–10 m of core YC01 on the Jiangsu tidal flats recorded a total of 36 TC-event-beds spanning from 645 to 1950 yr BP, with a high sedimentation rate of 6.5 mm/yr on average and a temporal resolution of grain-size parameters at 4 cm spacing of about 6 years. Meanwhile, the upper 192 cm of offshore core ZM01, dated between approximately 1910 yr BP and −68 yr BP, has a temporal resolution of grain-size analyses at 1 cm spacing of about 10 years. The study period of 645 to 1910 yr BP was therefore selected to cover the overlap of the two records. Moreover, the stable sedimentary environments in the Jiangsu tidal flats and Zhejiang-Fujian mud belt, including tidal regime over the past 2 kyr[30,45] permit the integration of longer TC intensity records into the instrumental record using the TCI_*fd* and TCI_*ws* indices.

The estimated TCI_*fd* and TCI_*ws* values, as well as the reconstructed TC intensity from[34], exhibited similar trends despite chronological uncertainty (Supplementary Fig. 4), with average values of 5.0 m and 29.8 m/s, respectively. However, there was significant variability in these values during the study period, ranging from 2.7 to 9.8 m and 20.1 to 40.1 m/s, respectively. Interestingly, both records provide compelling evidence of a regime shift in TC intensity occurring at approximately 1440 and 1530 yr BP, respectively (Figs. 3 and S4), as detected by the popular iterated cumulative sums of squares algorithm[46]. Before this shift, the TCI_*fd* and TCI_*ws* varied from higher levels (6.4 m and 35.2 m/s on average) with a decreasing trend with time, but then abruptly decreased to lower levels (4.0 m and 27.5 m/s on average) with a more uniform distribution continuing to 645 yr BP. As a result of this shift, the average values of TCI_*fd* and TCI_*ws* have decreased by approximately 38% and 22%, respectively. It is worth noting that their maximum values never returned to the pre-shift average. Based on these two independent records, we conclude that the shift in TC intensity in eastern China occurred during an interval of approximately 1440–1530 yr BP, centered on approximately 1485 ± 45 yr BP. Following the shift, TC intensity in eastern China decreased ~30 ± 8% compared to that of pre-shift. The TCs in the northwestern Pacific exhibit large spatial inhomogeneity, with four clusters of TCs identified following different tracks[47]. The core sites

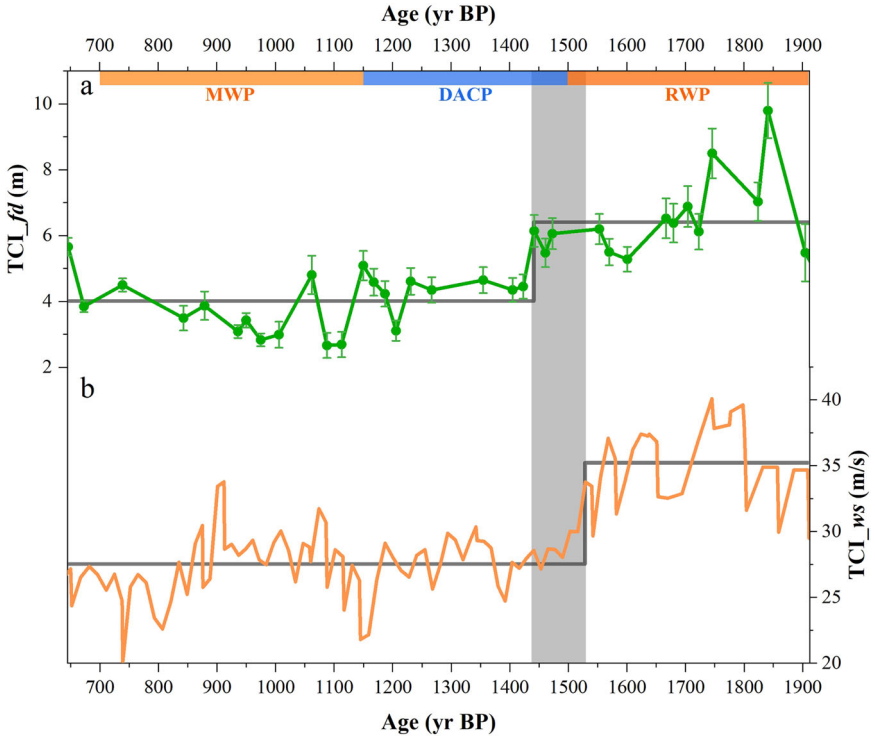

Fig. 3 | Late Holocene TC intensity records in eastern China. Comparison of TC intensity between (**a**) Jiangsu coast and (**b**) Zhejiang coast. The gray line and gray bar show the trend and regime shift in TC intensity, respectively. RWP Roman Warm Period (~2200–1500 yr BP), DACP Dark Ages Cold Period (~1500–1150 yr BP), MWP Medieval Warm Period (~1150–700 yr BP).

along the Zhejiang and Jiangsu coasts are primarily influenced by TCs belonging to cluster 1, which account for ~34% of the northwestern Pacific TCs. These TCs generally travel in a northwest-to-northwards direction and predominantly make landfall over East Asia. As a result, we infer that the variations in TC intensity near our sites reflect the changes in the intensity of TCs affecting the east coast of China north of Zhejiang and, to some extent, the average intensity variation of cluster 1 TCs in the northwestern Pacific.

According to the TCI_*fd* reconstruction, two TC-event-beds along the Jiangsu coast occurring around approximately 1745 and 1840 yr BP (i.e., TCI_*fd* of 8.5 and 9.8 m) seem to be linked to anomalously large TC events (Fig. 3a). The TC intensity associated with these events exceeds that of recent TCs observed since 1949 CE, as the instrumental maximum TC flow depth recorded along the Jiangsu coast is only 7.4 m[48]. However, there is no evidence of an anomalously large TC event with TCI_*ws* greater than the instrumental maximum TC wind speed affecting the Zhejiang coast (Fig. 2a). This suggests that the present TC wind speed impacting the Zhejiang coast, with a maximum of 42.5 m/s, is considerably higher than the maximum reconstructed TCI_*ws* of only 40.1 m/s over the past 2,000 years (Figs. 2a and 3b). Nonetheless, the onset of the highest TCI_*ws* values of 40.1 m/s and 39.6 m/s in Zhejiang coast aligns with the timing of these two anomalously large TCI_*fd* values in Jiangsu coast, which took place approximately 1745 and 1780 yr BP, respectively. Consequently, relying solely on instrumental or sedimentary evidence to assess the threat of TCs to coastal communities may significantly reduce the accuracy of such assessments. The inconsistency between the two reconstructions also highlights the importance of understanding TC activity on an inter-regional scale, which is critical to ensuring the safety of life and property in coastal communities.

Discussion

Theoretically, Emanuel (1987) proposed that the maximum potential intensity of TCs would increase in a greenhouse gas-warming climate[49]. Furthermore, observations and modeling support the 'temperature-TC intensity' paradigm, indicating that TC intensity should increase with Anthropogenic climate warming due to the rise in sea surface temperature (SST)[8,11,34,50]. SSTs in the low-latitude region are believed to be significant factors that influence TC intensity in the northwestern Pacific, as they determine the rate and duration of TC intensification[10,47]. Our record of TC intensity covers a sufficiently wide range of time and temperature to test this paradigm. Our two TC intensity indices, along with the tropical SST reconstructions from the Indo-Pacific warm pool, reveal that the highest reconstructed TCI_*fd* and TCI_*ws* both occur during the middle phase of the RWP (Fig. 3). Additionally, the observed 1485 ± 45 yr BP shift in TC intensity corresponds to the transition from the RWP to the DACP. However, this shift does not occur during the transition from the DACP to the MWP (Fig. 4a). Notably, there was no significant change in tropical SST magnitude before and after the 1485 ± 45 yr BP shift. For instance, while SST returned to and exceeded its pre-shift level during the late MWP (i.e., 700–950 yr BP), the TC intensity remained low. This makes it difficult to attribute the intensity shift to the temperature paradigm, as tropical SST did not undergo a shift before and after 1485 ± 45 yr BP. This is in line with observational studies, which suggest that the thermodynamic effect of the tropical SST alone cannot account for the documented changes in TC intensity (i.e., the annual accumulated power dissipation index) over the past 30 years[51]. Instead, this finding raises questions about whether other key large-scale climatic factors altered the state of TC intensity at around 1485 ± 45 yr BP. Studies relying on sedimentary archives indicate that long-term variations in the frequency, intensity and track of TC activity are tied with some key large-scale oceanic and atmospheric factors, such as El Niño–Southern Oscillation (ENSO), the Atlantic Meridional Overturning Circulation (AMOC), and the Sahara and West African Monsoon (WAM) (e.g., refs. 21,22,45,52–54). Reconstructions of past climate show some shifts in the magnitude of these factors during the past 2000 years (e.g., refs. 55–61), which may have caused a shift in TC intensity along the east coast of China. To test this hypothesis, we compared the reconstructions of TC intensity with proxy records of these factors.

ENSO is widely recognized as one of the primary drivers of global TC variability, significantly impacting TC activity in the northwestern Pacific, Australia, and the North Atlantic[27]. During El Niño years, when SSTs in the central and eastern equatorial Pacific are higher than normal, the mean genesis location for TCs in the northwestern Pacific generally shifts to the southeast, resulting in longer lifetime and greater intensity of TCs; In La Niña years, there is a tendency toward more short-lived TCs, many of which do

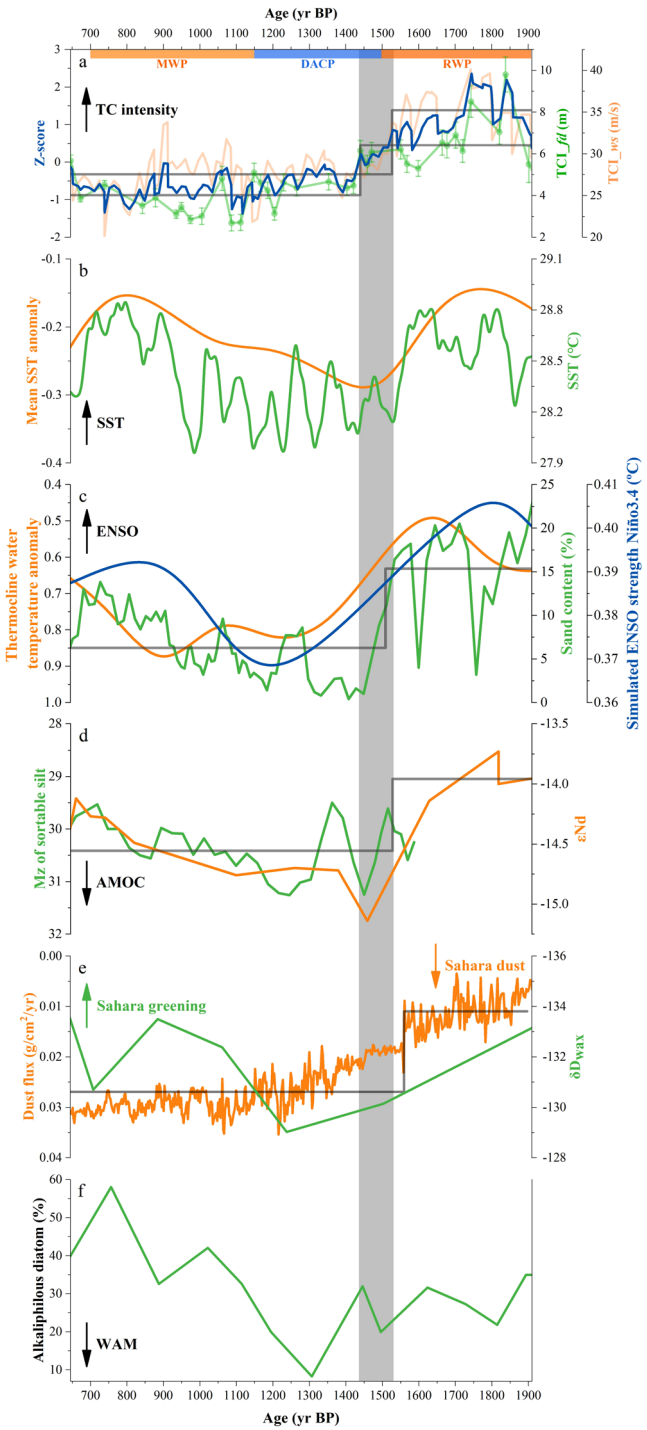

Fig. 4 | Comparisons of TC intensity reconstructions with other paleoclimatic records. a TC intensity from the Jiangsu and Zhejiang coasts. *Z*-score was realized by averaging the *Z*-cores of these two records. **b** SST reconstructions from the Indo-Pacific warm pool[55,89] (**c**) Reconstructed ENSO from the equatorial Pacific[55,56] and the TRACE simulation[90]. **d** AMOC reconstructions from the Bermuda Rise[57] and northern Iceland Basin[58]. **e** Reconstructed Saharan dust and vegetation from West and East Africa[59,60]. **f** Reconstruction of the WAM from equatorial Cameroon[61]. The gray bar shows the shift in TC intensity in eastern China. The shifts in the magnitude of ESNO, AMOC, and Saharan dust were detected using the popular iterated cumulative sums of squares algorithm[46].

not reach high TC intensity[62,63]. Based on the best-track dataset for the northwestern Pacific region for the period 1950–2002 CE, Camargo and Sobel (2005) suggested that the lifetime, intensity, and number of TCs contribute significantly to the ENSO signal in TC intensity, although the lifetime effect appears to be the most important of the three[63]. It seems that we can speculate that the mean lifetime of TCs tends to increase during El Niño phase as more TCs form in the southeast quadrant of the northwestern Pacific region. As a result, TCs will experience a longer traveling time (westward and northward) before encountering the continent or colder mid-latitude water, giving them a greater chance to develop higher intensity. Favorable atmospheric conditions (e.g. greater vorticity and weaker vertical wind shear) also exist in the southeast quadrant of the northwestern Pacific during El Niño years, which favor TC intensification[64]. However, the intensity effect in particular could also be due, to some extent, to other influences of ENSO on the mean regional climate of the northwestern Pacific[63]. Recent research has shown that during El Niño years, upper ocean heat content decreases by as much as 20%–30% (as compared to normal) over the northwestern Pacific[65]. This offsets the favorable atmospheric conditions and longer tracks, but the end result is still a slightly higher than normal TC intensity during El Niño years. Additionally, the AMOC plays a crucial role in redistributing heat on Earth and has a major impact on climate. Observational and modeling studies suggest that the weakening of AMOC leads to strong ENSO variability through the background warming over the central equatorial Pacific, resulting in an El Niño-like pattern in the tropical Pacific[66–68]. This pattern also contributes to the enhancement of TC intensity in the northwestern Pacific region. Our reconstructions demonstrate a consistent relationship between higher TC intensity and the strengthening of ENSO, as well as the weakening of AMOC (Fig. 4c, d), as evidenced by the observational data[63,68]. Specially, prior to the 1485 ± 45 yr BP shift, a gradual decrease in TC intensity is linked with a gradual decrease and increase in ENSO and AMOC, respectively. Conversely, lower and stable TC intensity after 1485 ± 45 yr BP coincides with weaker ENSO and stronger AMOC. Additionally, the slight increase in TC intensity after the 1485 ± 45 yr BP shift is coeval with a slight increase and decrease in ENSO and AMOC, respectively. It is noteworthy that the magnitude of ENSO and AMOC did not return to their pre-shift levels after 1485 ± 45 yr BP, suggesting that they are potentially key factors controlling the shift in TC intensity along the east coast of China.

Observational and numerical simulations have shown that vegetation cover and dust emission over the Sahara can impact TC intensity by triggering changes in the atmospheric circulation that affect the entire tropical region[52,54,69]. Their results suggest that TC intensity is positively correlated with Sahara vegetation and negatively correlated with Saharan dust concentration, both of which provide more favorable conditions for TC development[52]. Studies have demonstrated that Saharan dust, acting as cloud condensation nuclei, can lead to a significant reduction in the intensity of an idealized TC; This reduction is caused by the redistribution of precipitation and latent heating to more vigorous convection in the storm periphery that cools the low levels and disrupts the inflow of energy to the eyewall, hence making the eye larger and the maximum winds weaker[69,70]. Previous studies have also indicated that approximately one quarter of dust cases in East Asia between 2007 and 2020 CE originating from the Sahara Desert[71], primarily distributed in the upper troposphere, influence TC intensity through aerosol-cloud-radiation interactions[70]. So that, prior to the shift in our TC intensity reconstruction, lower Saharan dust emissions were associated with higher TC intensity (Fig. 4a, e), which is consistent with mid-Holocene TC modeling studies[52]. The relatively stable and high Saharan dust emissions after 1485 ± 45 yr BP may have contributed to TC intensity remaining at a low level, also in line with our intensity reconstructions. Furthermore, the magnitude of Saharan dust after the shift did not return to pre-shift levels, suggesting its potential role in controlling this intensity shift.

A gradual decrease and subsequent increase in Sahara greening before and after the 1485 ± 45 yr BP shift would result in corresponding changes in TC intensity, which can roughly explain the trends in our TC intensity records. However, the magnitude of Sahara greening did not produce a significant change before and after the shift, which would not account for the significant shift between higher and lower TC intensity (Fig. 4a, e). Notably, the greening of the Sahara reached its peak around 900 yr BP, but TC intensity did not reach its highest level during that time. This contrasts with the findings of Pausata et al.[52], which suggest that the impact of Sahara greening is more significant for TC activity than the role of reduced dust loadings. Pausata et al.[52] examined the effect of Sahara greening and dust on TC activity during a warm climate state (mid-Holocene, 6000 yr BP) characterized by increased boreal summer insolation, while our TC intensity records focus on the past two millennia marked by decreased boreal summer insolation. The different climate state may cause the role of Sahara greening and dust on TC activity to vary across different time scales. For instance, the influence of Saharan dust on TC activity in the North Atlantic varies at different time scales[54], suggesting that substantial increases in Saharan dust over the last 200 years and in the early Holocene are coeval with higher Atlantic TC activity, but are inversely correlated at other times over the last 3000 years.

Previous studies have also shown a correlation between the strength of WAM and TC intensity, suggesting that an intensified WAM increases TC intensity by enhancing cyclonic vorticity[21,52,72]. This correlation is consistent with our reconstructions, linking higher TC intensity before the 1485 ± 45 yr BP shift with a stronger WAM (Fig. 4a, f). However, the gradual weakening of the WAM after the shift contradicts our TC intensity records, as it would lead to a corresponding decrease in TC intensity. For example, the WAM reaches a maximum around 1300 yr BP within the study interval, but the corresponding TC intensity does not follow this trend. In addition, recent observational diagnostics and numerical simulations by Xu et al.[73] show that the increasing intensity of TCs in the northwestern Pacific over the past decades is partly driven by the warming of the central-eastern Tibetan Plateau by reducing vertical wind shear within the monsoon trough area of the tropical northwestern Pacific. However, after comparing our reconstructed TC intensity with the temperature record from the central-eastern Tibetan Plateau over the past two millennia (ref. 74; Supplementary Fig. 5), we have observed that increased TC intensity in eastern China corresponds to the warming of the Tibetan Plateau, particularly since 1600 yr BP. However, it is not the primary factor driving the shift in TC intensity around 1485 ± 45 yr BP, as its temperature did not shift at the same time. The aforementioned lines of evidence suggest that Sahara greening, the WAM, and the temperature of the Tibetan Plateau are unlikely to be the key factors controlling the shift in TC intensity in eastern China.

In summary, this study presents a late Holocene record of TC intensity in eastern China using an instrumental-calibrated technique, which allows for the calibration of long-term records against high-resolution instrumental TC records. The record reveals a significant regime shift in TC intensity around 1485 ± 45 yr BP along the east coast of China, marked by a 30 ± 8% reduction in intensity. This reduction can be attributed to substantial changes in the magnitudes of ENSO, AMOC, and Saharan dust, which may compensate for the effects of the 'temperature-TC intensity' paradigm. Moreover, as we assess the impacts of climate change, there is an increasing focus on "tipping elements" –components of the Earth's climate system where state shifts are likely to occur[75]. Interestingly, all three factors that we proposed to influence the shift of TC intensity belong to these tipping elements of the climate[76–78]. It is suggested that ENSO, AMOC, and Saharan dust may have crossed a similar tipping point around 1485 ± 45 yr BP, as their magnitudes have not returned to their pre-shift levels since then. This may have resulted in their influence on TC intensity exceeding that of temperature by triggering changes in the oceanic and atmospheric state within the tropical Pacific the region where TCs originate. These findings highlight the importance of understanding TC intensity variability over long time scales and under different climatic conditions. Further research is needed to evaluate TC intensity variability at different time scales in different basins and globally, as well as its connection with climate tipping elements. Additionally, the instrumental-calibrated technique offers the possibility of predicting future trends in TC activity under changing climate conditions. It enables the assessment of changes in TC activity from a long-term perspective, allowing for the discrimination between natural variability and anthropogenic changes in TC activity. We expect this technique to serve as a starting point for more accurate and quantitative analysis of paleotempestology and other paleoclimatology on a global scale.

Methods

Study site and field sampling

The study focuses on the Jiangsu tidal flats and Zhejiang-Fujian mud belt (Fig. 1), located on the eastern coast of China, as these areas frequently intersect with TC paths. Core ZM01 (28°41.4′ N, 122°24.6′ E) is 5.08-m-long core was collected from the Zhejiang-Fujian mud belt in 2018 CE (Fig. 1a). Core YC01 (33°23.2′N, 120°12.3′E) and core SA (33°34.7′N, 120°33.3′E) are 39.75-m-long and 1.93-m-long cores, respectively, recovered from the Jiangsu coastal plain and modern tidal flats in 2014 CE (Fig. 1b). Additionally, two sections of the Jiangsu modern tidal flats (Fig. 1b) were surveyed in 2008 CE (section P1) and 2009 CE (section P2) using a Magellan Z-MAX GPS-RTK (a differential GPS system with a dynamic accuracy of 10 mm ± 0.5 ppm), resulting in high-precision positional data. Thirty-seven surficial sediment samples were also collected along these two sections.

Laboratory analysis

Cores ZM01, YC01, and SA were sliced into intervals of 1 cm, 4 cm, and 1 cm, respectively. All subsamples from the three cores and thirty-seven surficial sediments were measured for grain size using a laser Malvern Mastersizer 2000 with a duplicate measurement error of less than 3%. Grain size parameters were then calculated from the distribution curves using moment statistics. The age model for cores ZM01, YC01, and SA, presented by Yang et al.[30,45], were established using two isotopic dating methods. Twenty-one and thirteen samples from the top of core ZM01 and core SA were selected for ^{210}Pb analysis to quantify the sedimentation rate. The centennial-to-millennial scale chronologies of cores ZM01 and YC01 were constrained using eight and seven ^{14}C-Accelerator Mass Spectrometry (^{14}C AMS) dates, respectively. The top 1 m of sediments in core YC01 consists of yellowish-brown sandy silt, belonging to the supratidal zone, which was insensitive to recording TC events and therefore was not included for analysis.

Determination of past TC intensity

Sedimentary systems in shelf-coastal environments, such as tidal flats and shelf mud belts, require different methods to delimit the intensity of TC-event-beds[79]. To address this issue and enable direct quantitative comparisons between instrumental and long-term TC records, we have developed two TC intensity indices for the Jiangsu tidal flats and Zhejiang-Fujian mud belt using a technique that combines instrumental and sedimentary records. This technique allows us to calibrate long-term records of past TC intensity against high-resolution instrumental TC records.

Jiangsu tidal flats. For the Jiangsu tidal flats, Yang et al.[30] presented a 2 kyr continuous activity record of TCs by identifying 36 coarse-grained event beds in core YC01. However, this work focused on revealing the frequency of TC-event-beds without quantifying the intensity of individual event beds. The magnitude of past TC-event-beds can be reproduced using a simple A-S model[31,80,81]. The A-S model is based on the balance between longitudinal sediment transport by the flow and gravity-driven sediment settling through the water column. It assumes that the distance that grains are advected longitudinally from the top of the flow to the bed depends on flow depth, flow velocity, and settling velocity[82]:

$$\frac{h}{w_s} = t = \frac{x_L}{U} \quad (1)$$

where h is flow depth during TC-induced flooding, w_s is the still–water particle settling velocity, t is settling time, and x_L is the advection length scale for particles of a given grain size. U is depth-averaged flow velocity and can be calculated using the equation in Moore et al.[82]. For a given grain size and shape, w_s can be calculated using equation in Ferguson and Church[83]. In this analysis, we determined the settling velocity for the D90 size class (defined as the grain size for which 90% of sample has smaller grain sizes) as it best reflects the maximum grain size transported by flooding events associated with TCs. The availability of coarse sand on the offshore sand ridges[84] presumably allows the assumption that D90 is controlled by flow.

The A-S model depends on the supercritical flow occurring along the backside of a barrier (i.e., Froude number $\mathrm{Fr} = \mathrm{U}/(gh)^{0.5} = 1$, g is acceleration due to gravity), but could theoretically apply to at any transition to supercritical flow, including tidal flat environments[42,85]. Woodruff et al.[31] assumed a constant x_L during storm surges to yield a unique solution for quantifying the flow depth over a barrier during flooding. This assumption is appropriate for environments where the topographic or bathymetric changes are insignificant over time, such as coastal lagoons and lakes[32,40,42]. However, in meso- to macro-tidal settings like Jiangsu tidal flats, water depths are variable, and sediment grain sizes differ in different parts of the tidal flats[86]. Therefore, a constant x_L is not suitable for calculating the flow depth during flooding in different parts of the tidal flats. As a result, Eq. 1 requires an additional water depth constraint to estimate the flow depth during flooding for different parts of the tidal flats (Supplementary Fig. 2).

To enhance the A-S model, we hypothesized that transport distance is dependent on water depth, as different parts of the tidal flats have varying x_L. By analyzing the TC-event-beds identified in core SA and the corresponding instrumented flow depths during TC-induced flooding[87,88], we were able to determine the transport distances for different parts of the Jiangsu tidal flats. Taking into account sea level variations, we can reconstruct the flow depth-based TC intensity (TCI_*fd*, *m*) recorded in core YC01 using the improved A-S model that incorporates different transport distances. The model can be expressed as follows:

$$\mathrm{TCI\_}fd = \left(\frac{{x_L}^2 {w_s}^2}{g}\right)^{1/3} \quad (2)$$

Zhejiang-Fujian mud belt. Yang et al.[45] developed a simple yet effective method for core ZM01 from the Zhejiang-Fujian mud belt by correlating sediment grain size with instrumental records of TC-induced wind speed. By combining the instrumental and sedimentary records, they discovered a significant and positive correlation ($R = 0.86$, $P < 0.001$, $n = 35$) between the content of the sensitive coarse-grained fraction (i.e., >63 μm fraction; sand content) in core ZM01 and the annual maximum wind speed of TCs that impacted the Zhejiang coast (120–124°E, 26–30°N) from 1984 to 2018 CE (Fig. 2a). However, the reconstruction of Yang et al.[45] based only on the sand content cannot directly quantify the intensity changes of TCs over the last 2000 years. To address this issue, we developed an index called the wind speed-based TC intensity index (TCI_*ws*, m/s), which is based on the relationship between the sand content and TC wind speed. The index can be expressed as follows:

$$\mathrm{TCI\_}ws = 6.3449^{*}\,\mathrm{LN}(\text{sand content}) + 31.52 \quad (3)$$

Data availability

All data needed to evaluate the conclusions in the paper are available at: https://doi.org/10.6084/m9.figshare.24258676.v1.

Received: 10 December 2023; Accepted: 22 April 2024;
Published online: 11 June 2024

References

1. Zhang, Q., Wu, L. & Liu, Q. Tropical cyclone damages in China 1983–2006. *Bull. Am. Meteorol. Soc* **90**, 489–496 (2009).
2. Peduzzi, P. et al. Global trends in tropical cyclone risk. *Nat. Clim. Change* **2**, 289–294 (2012).
3. Coronese, M., Lamperti, F., Keller, K., Chiaromonte, F. & Roventini, A. Evidence for sharp increase in the economic damages of extreme natural disasters. *Proc. Natl Acad. Sci. USA* **116**, 21,450–21,455 (2019).
4. Knutson, T. R. et al. Tropical cyclones and climate change. *Nat. Geosci* **3**, 157–163 (2010).
5. Emanuel, K. A. Downscaling CMIP5 climate models shows increased tropical cyclone activity over the 21st century. *Proc. Natl Acad. Sci. USA* **110**, 12219–12224 (2013).
6. Bacmeister, J. et al. Projected changes in tropical cyclone activity under future warming scenarios using a high–resolution climate model. *Clim. Change* **146**, 547–560 (2018).
7. Chand, S. S. et al. Declining tropical cyclone frequency under global warming. *Nat. Clim. Change* **12**, 655–661 (2022).
8. Emanuel, K. Increasing destructiveness of tropical cyclones over the past 30 years. *Nature* **436**, 686–688 (2005).
9. Webster, P. J., Holland, G. J., Curry, J. A. & Chang, H. R. Changes in tropical cyclone number, duration, and intensity in a warming environment. *Science* **309**, 1844–1846 (2005).
10. Mei, W., Xie, S. P., Primeau, F., McWilliams, J. C. & Pasquero, C. Northwestern Pacific typhoon intensity controlled by changes in ocean temperatures. *Sci. Adv* **1**, e1500014 (2015).
11. Bender, M. A. et al. Modeled impact of anthropogenic warming on the frequency of intense Atlantic hurricanes. *Science* **327**, 454–458 (2010).
12. Knutson, T. R. et al. Global projections of intense tropical cyclone activity for the late twenty–first century from dynamical downscaling of CMIP5/RCP4.5 scenarios. *J. Clim.* **28**, 7203–7224 (2015).
13. Goldenberg, S. B., Landsea, C. W., Mestas–Nuñez, A. M. & Gray, W. M. The recent increase in Atlantic hurricane activity: Causes and implications. *Science* **293**, 474–479 (2001).
14. Chan, J. C. Comment on" Changes in tropical cyclone number, duration, and intensity in a warming environment". *Science* **311**, 1713–1713 (2006).
15. Klotzbach, P. J. et al. Trends in global tropical cyclone activity: 1990–2021. *Geophys. Res. Lett* **49**, e2021GL095774 (2022).
16. Landsea, C. W., Harper, B. A., Hoarau, K. & Knaff, J. A. Can we detect trends in extreme tropical cyclones? *Science* **313**, 452–454 (2006).
17. Knutson, T. et al. Tropical cyclones and climate change assessment: Part I: Detection and attribution. *Bull. Am. Meteorol. Soc* **100**, 1987–2007 (2019).
18. Knutson, T. et al. Tropical cyclones and climate change assessment: Part II: projected response to anthropogenic warming. *Bull. Am. Meteorol. Soc* **101**, E303–E322 (2020).
19. Liu, K. B. & Fearn, M. L. Lake–sediment record of late Holocene hurricane activities from coastal Alabama. *Geology* **21**, 793–796 (1993).
20. Nott, J. & Hayne, M. High frequency of 'super–cyclones' along the Great Barrier Reef over the past 5,000 years. *Nature* **413**, 508–512 (2001).
21. Donnelly, J. P. & Woodruff, J. D. Intense hurricane activity over the past 5,000 years controlled by El Niño and the West African monsoon. *Nature* **447**, 465–468 (2007).
22. Chen, H. F. et al. Strengthening of paleo-typhoon and autumn rainfall in Taiwan corresponding to the Southern Oscillation at late Holocene. *J. Quat. Sci* **27**, 964–972 (2012).
23. Chen, H. F. et al. China's historical record when searching for tropical cyclones corresponding to Intertropical Convergence Zone (ITCZ) shifts over the past 2 kyr. *Clim. Past* **15**, 279–289 (2019).
24. Yue, Y. et al. 3500–year western Pacific storm record warns of additional storm activity in a warming warm pool. *Palaeogeogr. Palaeoclimatol. Palaeoecol.* **521**, 57–71 (2019).

25. Green, A. N. et al. Stormier mid–Holocene southwest Indian Ocean due to poleward trending tropical cyclones. *Nat. Geosci* **15**, 60–66 (2022).
26. Woodruff, J. D., Donnelly, J. P. & Okusu, A. Exploring typhoon variability over the mid–to–late Holocene: evidence of extreme coastal flooding from Kamikoshiki, Japan. *Quat. Sci. Rev* **28**, 1774–1785 (2009).
27. Nott, J. & Forsyth, A. Punctuated global tropical cyclone activity over the past 5,000 years. *Geophys. Res. Lett.* **39**, 14703 (2012).
28. Oliva, F., Viau, A. E., Peros, M. C. & Bouchard, M. Paleotempestology database for the western North Atlantic basin. *Holocene* **28**, 1664–1671 (2018).
29. Tao, S. et al. Poleward shift in tropical cyclone tracks in the Northwest Pacific during warm periods: Past and future. Paleoceanogr. *Paleoclimatol* **36**, e2021PA004367 (2021).
30. Yang, Y. et al. A late Holocene shift of typhoon activity recorded by coastal sedimentary archives in eastern China. *Sedimentology* **69**, 954–969 (2022).
31. Woodruff, J. D., Donnelly, J. P., Mohrig, D. & Geyer, W. R. Reconstructing relative flooding intensities responsible for hurricane–induced deposits from Laguna Playa Grande, Vieques, Puerto Rico. *Geology* **36**, 391–394 (2008).
32. Wallace, D. J. & Anderson, J. B. Evidence of similar probablility of intense hurricane strikes for the Gulf of Mexico over the late Holocene. *Geology* **38**, 511–514 (2010).
33. Brandon, C. M., Woodruff, J. D., Lane, D. P. & Donnelly, J. P. Tropical cyclone wind speed constraints from resultant storm surge deposition: a 2500 year reconstruction of hurricane activity from St. Marks, FL. *Geochem., Geophys., Geosyst* **14**, 2993–3008 (2013).
34. Zhou, X. et al. Enhanced tropical cyclone intensity in the western North Pacific during warm periods over the last two millennia. *Geophys. Res. Lett* **46**, 9145–9153 (2019).
35. Liu, K. B. *Hurricanes and Typhoons: Past, Present, and Future*. (eds. Murnane R. J., Liu K. B.) p. 13-57 (Columbia University Press, 2004).
36. Nott, J. Palaeotempestology: the study of prehistoric tropical cyclones—a review and implications for hazard assessment. *Environ. Int.* **30**, 433–447 (2004).
37. Donnelly, J. P. et al. Climate forcing of unprecedented intense-hurricane activity in the last 2000 years. *Earth's Future* **3**, 49–65 (2015).
38. Liu, K. B. & Fearn, M. L. Reconstruction of prehistoric landfall frequencies of catastrophic hurricanes in northwestern Florida from lake sediment records. *Quat. Res.* **54**, 238–245 (2000).
39. Nott, J. F. Intensity of prehistoric tropical cyclones. *J. Geophys. Res. Atmos.* **108**, 4212 (2003).
40. Brandon, C. M., Woodruff, J. D., Donnelly, J. P. & Sullivan, R. M. How unique was Hurricane Sandy? Sedimentary reconstructions of extreme flooding from New York Harbor. *Sci. Rep* **4**, 1–9 (2014).
41. Hong, I. et al. Sedimentological characteristics of the 2015 tropical cyclone pam overwash sediments from Vanuatu, South Pacific. *Mar. Geol.* **396**, 205–214 (2018).
42. Bregy, J. C., Wallace, D. J., Minzoni, R. T. & Cruz, V. J. 2500–year paleotempestological record of intense storms for the northern Gulf of Mexico, United States. *Mar. Geol.* **396**, 26–42 (2018).
43. Gao, S. et al. Holocene sedimentary systems on a broad continental shelf with abundant river input: process–product relationships. *Geol. Soc. Spec. Publ.* **429**, 231–268 (2016).
44. Yang, R. & Xie, Z. R. Sea–level changes along the east coast of China over the last 20,000 years. *Oceanol. Limnol. Sin.* **15**, 1–13 (1984). (In Chinese).
45. Yang, Y. et al. Northwestern Pacific tropical cyclone activity enhanced by increased Asian dust emissions during the Little Ice Age. *Nat. Commun.* **13**, 1712 (2022).
46. Inclan, C. & Tiao, G. C. Use of cumulative sums of squares for retrospective detection of changes of variance. *J. Am. Stat. Assoc.* **89**, 913–923 (1994).
47. Mei, W. & Xie, S. P. Intensification of landfalling typhoons over the northwest Pacific since the late 1970s. *Nat. Geosci.* **9**, 753–757 (2016).
48. Ren, M. E., Zhang, R. S., Yang, J. H. & Zhang, D. C. The influence of storm tide on mud plain coast-with special reference to Jiangsu Province. *Mar. Geol. Quat. Geol.* **3**, 1–24 (1983).
49. Emanuel, K. A. The dependence of hurricane intensity on climate. *Nature* **326**, 483–485 (1987).
50. Yan, Q. et al. Enhanced intensity of global tropical cyclones during the mid-Pliocene warm period. *Proc. Natl Acad. Sci. USA* **113**, 12963–12967 (2016).
51. Wu, L., Wang, B. & Braun, S. A. Implications of tropical cyclone power dissipation index. *Int. J. Climatol.* **28**, 727–731 (2008).
52. Pausata, F. S. Tropical cyclone activity enhanced by Sahara greening and reduced dust emissions during the African Humid Period. *Proc. Natl Acad. Sci. USA* **114**, 6221–6226 (2017).
53. Toomey, M. R., Korty, R. L., Donnelly, J. P., van Hengstum, P. J. & Curry, W. B. Increased hurricane frequency near Florida during Younger Dryas Atlantic Meridional Overturning Circulation slowdown. *Geology* **45**, 1047–1050 (2017).
54. Hayes, C. T. & Wallace, D. J. Exploring records of Saharan dust transport and hurricanes in the western North Atlantic over the Holocene. *Quat. Sci. Rev* **205**, 1–9 (2019).
55. Dang, H. et al. Pacific warm pool subsurface heat sequestration modulated Walker circulation and ENSO activity during the Holocene. *Sci. Adv* **6**, eabc0402 (2020).
56. Conroy, J. L., Overpeck, J. T., Cole, J. E., Shanahan, T. M. & Steinitz-Kannan, M. Holocene changes in eastern tropical Pacific climate inferred from a Galápagos lake sediment record. *Quat. Sci. Rev.* **27**, 1166–1180 (2008).
57. Lippold, J., Rheinberger, S. & Jaccard, S. L. Constraining the variability of the Atlantic meridional overturning circulation during the Holocene. *Geophys. Res. Lett.* **46**, 11338–11346 (2019).
58. Spooner, P. T. et al. Exceptional 20th century ocean circulation in the northeast Atlantic. *Geophys. Res. Lett* **47**, e2020GL087577 (2020).
59. Mulitza, S. et al. Increase in African dust flux at the onset of commercial agriculture in the Sahel region. *Nature* **466**, 226–228 (2010).
60. Tierney, J. E. & DeMenocal, P. B. Abrupt shifts in Horn of Africa hydroclimate since the Last Glacial Maximum. *Science* **342**, 843–846 (2013).
61. Nguetsop, V. F., Servant-Vildary, S. & Servant, M. Late Holocene climatic changes in west Africa, a high resolution diatom record from equatorial Cameroon. *Quat. Sci. Rev.* **23**, 591–609 (2004).
62. Chan, J. C. Tropical cyclone activity in the northwest Pacific in relation to the El Niño/Southern Oscillation phenomenon. *Mon. Weather Rev* **113**, 599–606 (1985).
63. Camargo, S. J. & Sobel, A. H. Western North Pacific tropical cyclone intensity and ENSO. *J. Clim.* **18**, 2996–3006 (2005).
64. Lin, I. I. et al. ENSO and tropical cyclones. El Niño Southern Oscillation in a changing climate. *Geophys. Monogr.* **253**, 377–408 (2020).
65. Zheng, Z. W., Lin, I. I., Wang, B., Huang, H.-C. & Chen, C. H. A long neglected damper in the El Niño–typhoon relationship: a 'Gaia-like'process. *Sci. Rep.* **5**, 11103 (2015).
66. Zhang, R. & Delworth, T. L. Simulated tropical response to a substantial weakening of the Atlantic thermohaline circulation. *J. Clim.* **18**, 1853–1860 (2005).
67. Kang, I. S., No, H. H. & Kucharski, F. ENSO amplitude modulation associated with the mean SST changes in the tropical central Pacific induced by Atlantic multidecadal oscillation. *J. Clim.* **27**, 7911–7920 (2014).
68. Zhang, R. et al. A review of the role of the Atlantic meridional overturning circulation in Atlantic multidecadal variability and associated climate impacts. *Rev. Geophys.* **57**, 316–375 (2019).

69. Zhang, H., McFarquhar, G. M., Saleeby, S. M. & Cotton, W. R. Impacts of Saharan dust as CCN on the evolution of an idealized tropical cyclone. *Geophys. Res. Lett*. **34**, L14812 (2007).
70. Liang, Z., Ding, J., Fei, J., Cheng, X. & Huang, X. Direct/indirect effects of aerosols and their separate contributions to Typhoon Lupit (2009): eyewall versus peripheral rainbands. *Sci. China Earth Sci.* **64**, 2113–2128 (2021).
71. Liu, Q., Huang, Z., Hu, Z., Dong, Q. & Li, S. Long-range transport and evolution of Saharan dust over East Asia from 2007 to 2020. *J. Geophys. Res. Atmos.* **127**, e2022JD036974 (2022).
72. Bell, G. D. & Chelliah, M. Leading tropical modes associated with interannual and multidecadal fluctuations in North Atlantic hurricane activity. *J. Clim.* **19**, 590–612 (2006).
73. Xu, J. et al. Increasing tropical cyclone intensity in the western North Pacific partly driven by warming Tibetan Plateau. *Nat. Commun.* **15**, 310 (2024).
74. Liu, Y., Cai, Q., Song, H., An, Z. & Linderholm, H. W. Amplitudes, rates, periodicities and causes of temperature variations in the past 2485 years and future trends over the central-eastern Tibetan Plateau. *Chin. Sci. Bull.* **56**, 2986–2994 (2011).
75. Armstrong-McKay, D. I. et al. Exceeding 1.5 C global warming could trigger multiple climate tipping elements. *Science* **377**, eabn7950 (2022).
76. Lenton, T. M. et al. Tipping elements in the Earth's climate system. *Proc. Natl Acad. Sci. USA* **105**, 1786–1793 (2008).
77. Kopp, R. E., Shwom, R. L., Wagner, G. & Yuan, J. Tipping elements and climate–economic shocks: pathways toward integrated assessment. *Earth's Future* **4**, 346–372 (2016).
78. Wang, S. et al. Mechanisms and impacts of Earth system tipping elements. Rev. Geophys. **61**, e2021RG000757 (2023).
79. Gao, S. & Collins, M. B. Holocene sedimentary systems on continental shelves. *Mar. Geol.* **352**, 268–294 (2014).
80. Johnson, J. P., Delbecq, K. & Kim, W. Predicting paleohydraulics from storm surge and tsunami deposits: using experiments to improve inverse model accuracy. *J. Geophys. Res. Earth Surf.* **122**, 760–781 (2017).
81. Wang, S., Ge, J., Meadows, M. E. & Wang, Z. Reconstructing a late Neolithic extreme storm event on the southern Yangtze coast, East China, based on sedimentary records and numerical modeling. *Mar. Geol.* **443**, 106687 (2022).
82. Moore, A. L., Mcadoo, B. G. & Ruffman, A. Landward fining from multiple sources in a sand sheet deposited by the 1929 Grand Banks Tsunami, Newfoundland. *Sediment. Geol.* **200**, 336–346 (2007).
83. Ferguson, R. I. & Church, M. A simple universal equation for grain settling velocity. *J. Sediment. Res.* **74**, 933–937 (2004).
84. Wang, Y., Zhang, Y., Zou, X., Zhu, D. & Piper, D. The sand ridge field of the South Yellow Sea: origin by river–sea interaction. *Mar. Geol.* **291**, 132–146 (2012).
85. Mullarney, J. C. & Henderson, S. M. Hydraulically controlled front trapping on a tidal flat. *J. Geophys. Res.: Oceans* **116**, C04023 (2011).
86. Reineck H.-E. & Singh I. B. *Depositional Sedimentary Environments.* 2nd edn. p. 549 (Springer, 1980).
87. Wang, H., Yao, S. K., Gong, M. S., Wu, H. M. & Shi, S. H. Analysis of data on the storm surge in the yangkou harbor, Jiangsu. *Mar. Sci. Bull.* **26**, 26–32 (2007). (In Chinese).
88. Yu, F. J., Dong, J. & X., Ye, L. Collection of storm surge disasters historical data in China 1949–2009. p. 743 (China Ocean Press, 2015). (In Chinese)
89. Oppo, D. W., Rosenthal, Y. & Linsley, B. K. 2,000-year-long temperature andhydrology reconstructions from the indo-pacific warm pool. *Nature* **460**, 1113–1116 (2009).
90. Liu, Z. et al. Evolution and forcing mechanisms of El Niño over the past 21,000 years. *Nature* **515**, 550–553 (2014).

Acknowledgements

This work was supported by the National Natural Science Foundation of China (No. 42276050-Y.Y., 41706096-L.Z., 41530962-S.G.), the Open Research Fund of State Key Laboratory of Estuarine and Coastal Research (No. SKLEC-KF202302-Y. Y), and the Open Research Fund of Key Laboratory of Coastal Salt Marsh Ecosystems and Resources (No. KLCSMERMNR2021001-Y. Y). David J. W. Piper (Geological Survey of Canada) and Min Xu reviewed and clarified the final manuscript in 2023. The authors thank Yangyang Zhao, Zhuochen Han, Qingguang Zhu, Qijun Yin, Qiao Ai, Peipei Zhao, Shengjing Liu, Chengfen Xue, Zhaoxiang Yang for their help with field sampling and laboratory analysis. The authors thank the two anonymous reviewers for their constructive comments, which improved the paper.

Author contributions

Y.Y., L.Z., and S.G. designed the study, wrote, and revised the paper. V.M. contributed to the development of the idea and the revision of the paper. J.H.G., Y.G., Y.P.W., and J.J.J. made suggestions for improving the quality of the paper. All the authors discussed and reviewed the paper prior to submission.

Competing interests

The authors declare no competing interests.

Additional information

Supplementary information The online version contains supplementary material available at https://doi.org/10.1038/s41612-024-00656-8.

Correspondence and requests for materials should be addressed to Liang Zhou or Shu Gao.